Supporting Information

López et al. 10.1073/pnas.1318754110

SI Materials and Methods

Purification of T4 Lysozyme Mutants from Inclusion Bodies. Isolation of T4 lysozyme (T4L) from inclusion bodies was done for all 121A/133A mutants as described by Liu et al. (1), with some modifications. After sonication of the crude extract and the subsequent centrifugation step, the pellet containing the inclusion body was washed with 20 mL of buffer consisting of 25 mM Tris base, 25 mM 3-(N-morpholino)propanesulfonic acid (MOPS), 0.1 mM EDTA, and 2% (vol/vol) Triton X-100 at pH 7.6. The mixture was sonicated on ice for 5 min. The resuspended pellet was incubated for 2 h at 4 °C, followed by centrifugation for 15 min at 26,892 × *g*. The pellet was collected and resuspended in 25 mL of buffer consisting of 50 mM Tris·Cl and 2.5% (vol/vol) of n-octyl-β-D-glucopyranoside at pH 8. The mixture was sonicated for 5 min, followed by incubation for 3 h at 4 °C. After another centrifugation step, the washed inclusion body pellet was resuspended in 20 mL of 10 mM glycine and the solution was sonicated for 5 min. Solid urea was added with vigorous stirring to a final concentration of 4 M, and the solution was quickly titrated to pH 3.0 with phosphoric acid to resolubilize the protein. The resolubilized protein was then subjected to a final centrifugation step to remove any remaining insoluble material, and the supernatant was dialyzed overnight against 2 L of a buffer consisting of 10 mM sodium citrate, 1 mM β-cyclodextrin, 15% (vol/vol) glycerol, and 5 mM DTT at pH 3.0. Another 1-d dialysis was done against 2 L of buffer with the same composition, except the pH was set to 5. After removal of precipitates, the refolded T4L protein was loaded into a Hi Trap CM FF ion exchange column (GE Healthcare) equilibrated with 10 mM sodium citrate and 5 mM DTT at pH 5.0. With a linear elution gradient of 0–400 mM NaCl, the T4L fraction eluted at 240 mM NaCl (conductivity of ~25 mS/cm). Sample purity was greater than 95%, as judged by SDS/PAGE electrophoresis. To ensure that there were no misfolded soluble oligomeric species in the sample, the T4L fraction was injected into a Superdex 75 (GE Healthcare) gel filtration column preequilibrated with 50 mM MOPS and 25 mM NaCl at pH 6.8. In all cases, there was a single peak with a retention volume of ~15.1 mL corresponding to monomeric T4L. Spin labeling of the T4L mutants was done as described previously (2).

Simulation of Electron Paramagnetic Resonance Spectra of Spin-Labeled T4L Mutants. Spectral simulations were performed using the program Multicomponent, version 705 (www.chemistry.ucla.edu/directory/hubbell-wayne-l), an interface based on LabView (National Instruments) that employs the non-linear least squares stochastic Liouville (NLSL) fitting program (ftp.ccmr.cornell.edu/pub/freed) as a kernel. Starting values for the principal components of the magnetic A and g tensors for solvent-exposed sites were A_{xx} = 5.7 G, A_{yy} = 6.0 G, A_{zz} = 37.5 G, g_{xx} = 2.0078, g_{yy} = 2.0058, and g_{zz} = 2.0023. These values are similar to those published earlier (3, 4), and they were used for all spectral components except where noted below. The tensor elements A_{zz} and g_{xx} are particularly sensitive to polarity, being smaller and larger, respectively, in a nonpolar environment compared with water (5). The electron paramagnetic resonance (EPR) spectra for R1 at some sites in the cavity mutants have a component corresponding to an immobilized nitroxide, where the nitroxide could be buried in a hydrophobic environment. This is apparently the case for the immobile components in T4L mutants 121A/133A for 128R1, 130R1, and 135R1, where A_{zz} = 35.5 and g_{xx} = 2.0088 were required for reasonable simulations of the spectra. These values are compatible with those previously determined for R1 buried in the hydrophobic interior of proteins (6, 7). Save for residue 123R1, the diffusion tilt for the mobile component was $\alpha_D = 0°$, $\beta_D = 36°$, and $\gamma_D = 0°$, although β_D was varied in the range of 25–40°. For 123R1, the diffusion tilt angles were αD = 0°, βD = 90°, and γD = −40°, which corresponds to an *x*-axis anisotropic motion (8).

The general strategy for fitting single- and multiple-component spectra using the macroscopic order microscopic disorder (MOMD) model has been described in detail (9–11). In the present application, the spectra of R1 in the WT protein are fit in a least-squares sense to the MOMD model with the motional parameters Rbar ($\overline{R}$), N, C_{20}, and C_{22} (in some cases) as parameters. Reasonable fits were obtained with an axially symmetrical motion, where $R_z \equiv R_\parallel$ and $R_x = R_y \equiv R_\perp$. In a modified spherical representation, the motion is specified by the geometric mean of the diffusion rate ($\overline{R}$) and the asymmetry parameter (N), where $\overline{R} = \sqrt[3]{R_\parallel R_\perp^2}$ and $N = \frac{R_\parallel}{R_\perp}$. The spectra of R1 at some sites in the WT protein show two components (e.g., 116R1 and 128R1); in such a case, the relative populations are also fitting parameters. To constrain the number of parameters for such sites, the relatively immobile components were taken to have isotropic motion, where $n = 1$. Least-square fits were obtained by variation of $\overline{R}$, N, and C_{20} only for the relatively mobile components and by variation of $\overline{R}$ only for the isotropic state. The 121A/133A cavity mutations introduced new components in the EPR spectra that correspond to immobilized states of R1, apparently without altering the components that characterize the WT protein, suggesting equilibrium between the states. To test this model, EPR for a composite of the WT protein and for a new state with an immobilized nitroxide was simulated and compared with the WT. For the simulation of R1 sites in the 121A/133A mutant, all magnetic and motional parameters obtained for the same sites in the WT protein were held constant and the motional parameters for the new component were varied, along with the populations of the WT and the new state. For cases where the WT spectra show two components, the ratio of the components and their motional parameters were invariant in the simulation. It is noted that the spectrum of W138A/N140R1 in the presence of phenol could not be simulated by keeping the motional parameters of 140R1 in the WT background constant; thus, $\overline{R}$, C_{20}, and C_{22} values were varied until a reasonable fit was obtained. Finally, the principal values of the A and g magnetic tensors were allowed to vary slightly to get the final best fits. From the final fits, the effective correlation time (τ) was calculated as $\tau = \frac{1}{6\overline{R}}$ and the order parameters (S_{20} and S_{22}) were computed directly from C_{20} and C_{22} (12).

Determination of Interspin Distances for N140R1/T151R1 in the WT and W138A Proteins with Continuous Wave Dipolar Broadening Methods. Interspin distances were measured at physiological temperatures in spin-labeling buffer, as described by Altenbach et al. (13). To determine the interspin distance, a reference EPR spectrum of the doubly labeled mutant in the absence of dipolar interaction (also known as "sum of singles") is obtained and compared with the experimental spectrum of the mutant to reveal the extent of dipolar broadening from which the distance (r) can be obtained. To obtain the sum of singles for 138A/140R1/151R1, the spectra of the singly labeled mutants (i.e., 138A/140R1, 138A/151R1) were recorded and normalized to the same numbers of spins and added. Analysis of the data was done using the program "ShortDistances" written in LabVIEW (National Instruments), which is available at www.chemistry.ucla.edu/directory/hubbell-wayne-l.

Thermal Unfolding of T4L Mutants. Thermal unfolding was monitored using the change ellipticity at 223 nm in the temperature

range of 15–80 °C or 20–80 °C for WT* using a heating rate of 2 °C/min. The concentration of the protein was in the range of 0.2–0.3 mg/mL. All measurements were done in buffer consisting of 20 mM phosphate and 25 mM KCl at pH 2.95. To evaluate the effect of halothane binding to the stability of the 121A/133A mutants, halothane was added to the protein via vapor diffusion, as described in *Materials and Methods*, and thermal denaturation was carried out immediately. Reversibility was checked by monitoring the ellipticity of the protein after the sample was cooled back to the initial temperature. The apparent melting temperatures (T_ms) were determined by direct fitting of the unfolding curve, as described by Greenfield (14). Briefly, the change in CD signal as a function of temperature can be analyzed using a nonlinear fitting to the following sets of equations:

$$\Delta G = \Delta H\left(1-\frac{T}{T_m}\right) - \Delta C_p\left((T_m - T) + T * ln\left(\frac{T}{T_m}\right)\right) \quad \textbf{[S1]}$$

$$K = e^{\left(-\frac{\Delta G}{RT}\right)} \quad \textbf{[S2]}$$

$$\alpha = \left(\frac{K}{1+K}\right) \quad \textbf{[S3]}$$

$$\theta_i = \alpha\left[\left(\theta_F + (A*T)\right) - \left(\theta_U + (B*T)\right)\right] + \left(\theta_U + (B*T)\right), \quad \textbf{[S4]}$$

where T is the temperature (Kelvin), T_m is the melting temperature, θ_i is the ellipticity at any temperature, θ_F is the ellipticity of the fully folded protein, θ_U is the ellipticity of the fully unfolded protein, and A and B are corrections terms for pre- and posttransition changes in ellipticity as a function of temperature. Examples of best fit of the raw data are shown in Fig. 6*A*. T_m values obtained from fits of the data were very similar (±0.3 °C) to those obtained from the first derivative curve of the raw data.

Estimating K_d from Ligand Titration Using EPR. As described in the main text, both the continuous wave (CW) EPR and double electron-electron resonance (DEER) data suggest the following model for ligand binding to the cavity mutants:

$$\begin{array}{ll} \mathrm{X} \leftrightarrow \mathrm{WT} & \mathrm{K_1} \\ \mathrm{WT} + \mathrm{L} \leftrightarrow \mathrm{WT{\bullet}L} & \mathrm{K_2} \end{array}$$

To estimate the value of the binding constant K_2, the following assumptions are made:

i) The EPR spectra of WT·L and WT are degenerate, that is, the conformation of the ligand-bound state is the same as the WT; this is supported by the CW spectral line shapes as a function of the ligand and the spectral simulations.
ii) The EPR spectrum of X is a pure immobilized state. The result is not strongly dependent on this assumption because the spectra of 128R1 and 135R1 are predominantly immobile, with only ≈10% of a mobile component [i.e., K_1 is apparently very small (128 $K_1 \approx 0.1$)].
iii) The presence of R1 in the WT conformation does not alter the binding of halothane.

The expression relating the equilibrium concentration of WT in the mixture to the equilibrium constants, the total ligand concentration (L_T), and the total protein concentration (P_T) is:

$$[\mathrm{WT}](1+\mathrm{K_1}) + [\mathrm{WT}](1+\mathrm{K_1}) + \mathrm{K_1K_2}[\mathrm{WT}][\mathrm{L_T}]/\left(1+[\mathrm{WT}]\mathrm{K_2}\right) = \mathrm{K_1P_T}. \quad \textbf{[S5]}$$

From the definition of the equilibrium constants and mass conservation for ligand and protein, the equilibrium concentrations of X and WT·L are obtained as a function of [WT]:

$$[\mathrm{WT{\bullet}L}] = [\mathrm{P_T}] - [\mathrm{WT}](1+1/\mathrm{K1}) \quad \textbf{[S6]}$$

$$[\mathrm{X}] = [\mathrm{WT}]/\mathrm{K1}. \quad \textbf{[S7]}$$

The CW EPR spectra of the equilibrium mixture of cavity mutant and ligand have two components, an immobilized state proportional to [X], and a mobile component corresponding to [WT] + [WT•L] (assumption 1 above and as discussed in main text). Addition of ligand then simply changes the fractions of each state, the values of which can be determined by globally fitting a set of spectra to a linear combination of the pure spectra corresponding to the individual states. The fraction of the mobile component (F_m), in terms of the model given above is:

$$[\mathrm{WT}] = [\mathrm{WT{\bullet}L}]/[\mathrm{P_T}] = \mathrm{F_m}. \quad \textbf{[S8]}$$

Eqs. **S5**–**S8** can be solved to provide an expression for F_m as a function of K_1, K_2, L_T, and P_T, and a fit of the experimental values for the fraction of mobile state to this expression provides values for K_1 and K_2; fits obtained in this way are shown in Fig. S5.

The value for the true ligand-binding constant thus determined, K_2, is substantially larger than the apparent binding constant, K_{app}, which does not recognize the existence of the conformational equilibrium:

$$\mathrm{K_{app}} = [\mathrm{WT{\bullet}L}]/\left([\mathrm{WT}] + [\mathrm{X}]\right)[\mathrm{L}] = \mathrm{K_2}/(1+1/\mathrm{K_1}) \quad \textbf{[S9]}$$

$$\mathrm{K_2} = \mathrm{K_{app}}(1+1/\mathrm{K_1}). \quad \textbf{[S10]}$$

Detecting Conformational Equilibria with Site-Directed Spin Labeling/EPR. The EPR spectra of R1 sensors in T4L reflect rotational diffusion of the nitroxide in the range of correlation times 100 ps < τ < 100 ns; this is the basic time window of X-band CW EPR spectroscopy. Both the order (S) and rates (τ^{-1}) of motion can be determined by fitting the spectra to a comprehensive theory of the line shape that includes anisotropic motions (12). The time scale for CW EPR conveniently overlaps that for fast backbone fluctuations, and the spectra of R1 in proteins can be analyzed to reveal the relative rates and amplitudes of picosecond-nanosecond backbone modes in helices (11, 15).

On the other hand, protein conformational exchange on a time scale of microseconds-milliseconds is outside the CW EPR time window, and no information on exchange rate is contained in the spectra. Nevertheless, the existence of conformational equilibria is revealed as multiple components in the EPR spectra, provided that R1 residues are positioned where they experience different environments in the conformers (16, 17). Unless there is local unfolding, one component is invariably immobilized, and a model to account for this result has been recently presented (11). Multiple component spectra can also arise from rotameric equilibria of R1, but methods have been developed to distinguish rotamer from conformational exchange (16–19). Of these strategies, saturation recovery (SR) and DEER can measure exchange rates on the microsecond time scale (17, 19). Finally, distance measurements between pairs of nitroxides using DEER spectroscopy can measure the amplitude of conformational fluctuations (20). Thus, site-directed spin-labeling/EPR can characterize both fast backbone motions and conformational flexibility with respect to both rate and amplitude.

Basic Principles and Procedures of Pulse SR EPR. The experimental procedure and instrumentation used for SR have been described

in detail by Bridges et al. (17). The typical sample volume was ~3 μL contained in a TPX capillary with an i.d. of 0.6 mm (Molecular Specialties, Inc.). All SR measurements were done at 295K under a nitrogen atmosphere in the absence of oxygen. The saturating pulse length was 1 μs, with an incident power of 250 mW. The observing power was 100 μW. Both the saturating and observing pulses were set to the maximum absorbance of the nitroxide $M_I = 0$ resonance (indicated by the dotted lines in Fig. 2). The number of points in each curve was 2,048, with a step size of 20 ns. The total number of acquisitions was 2.1 million (average acquisition time was 8–10 min). The reported relaxation time (T_1) values in this work were obtained by fitting experimental SR curves to mono- or biexponential functions using Origin 6.0 (OriginLab).

SR measures the electron spin lattice T_1 of a nitroxide. In the SR experiment, a saturating pulse of microwave radiation is delivered at a selected frequency and the recovery of magnetization is monitored as a function of time at the same frequency. For a nitroxide in a single environment (i.e., with a one-component spectrum), the recovery curve is a single exponential with a time constant of T_1. If the nitroxide is in physical exchange between two environments with resolved spectral components and different intrinsic T_1s, there are two limiting cases determined by whether the exchange rate is fast or slow compared with the difference in the intrinsic $(T_1)^{-1}$ values. If the exchange is fast, the recovery is a single exponential, with a reciprocal time constant given by the population-weighted average of the $(T_1)^{-1}$ values; if it is slow, the recovery is biexponential, with time constants given by the individual T_1s. For intermediate cases, exchange lifetimes in the range of 1–70 μs can be determined (17). In earlier work, it was found that the SR curve for multicomponent spectra arising from R1 rotamer exchange is monoexponential, indicating fast exchange, whereas protein conformational exchange on the microsecond-millisecond time scale gives rise to biexponential relaxations as expected for exchange rates slow on the T_1 time scale (17). In addition to information on exchange rates, the SR data provide R1 solvent accessibility measured by the collision frequency with the paramagnetic relaxation reagent nickel ethylenediaminediacetate (NiEDDA) (17, 21).

In the present study, sites 123R1 (G helix) and 128R1 (H helix) in the 121A/133A cavity mutant showing two-component EPR spectra and corresponding biexponential SR curves were analyzed. With six concentrations of NiEDDA in the range of 0–1.5 mM, analysis of the data according to the method of Bridges et al. (17) showed that the exchange lifetimes were slow on the above time scale (i.e., >70 μs) and a specific lifetime could not be determined. Nevertheless, the analysis provides the solvent accessibility of the nitroxide (J) in each state corresponding to the two conformations. The solvent accessibility of R1 at a particular site is defined as the collision frequency of the spin label with the polar relaxation reagent NiEDDA, and it is given in units of megahertz per millimolar with respect to the concentration of NiEDDA (21). For the other sites investigated with two-component spectra and biexponential relaxations (116R1, 131R1, and 135R1), exchange was assumed to be slow, as for 123R1 and 128R1, and J was determined from the two values of T_1 obtained from each SR relaxation curve in the presence of 0 and 1.5 mM NiEDDA according to $J = [T_1^{-1}(\text{NiEDDA}) - T_1^{-1}(0)]/1.5$ (21). For reference, typical values of J for R1 at solvent-exposed and buried sites are ~0.20 ± 0.03 and ≤0.001 MHz/mM, respectively (21). For sites with single exponential relaxations (131R1 and 140R1 in W138A T4L), J was determined according to the above equation using the single values of T_1 found in the presence and absence of 1.5 mM NiEDDA. All SR data are presented in Table S2.

1. Liu L, Baase WA, Michael MM, Matthews BW (2009) Use of stabilizing mutations to engineer a charged group within a ligand-binding hydrophobic cavity in T4 lysozyme. *Biochemistry* 48(37):8842–8851.
2. Mchaourab HS, Lietzow MA, Hideg K, Hubbell WL (1996) Motion of spin-labeled side chains in T4 lysozyme. Correlation with protein structure and dynamics. *Biochemistry* 35(24):7692–7704.
3. Columbus L, Kálai T, Jekö J, Hideg K, Hubbell WL (2001) Molecular motion of spin labeled side chains in alpha-helices: Analysis by variation of side chain structure. *Biochemistry* 40(13):3828–3846.
4. Liang Z, Lou Y, Freed JH, Columbus L, Hubbell WL (2004) A multifrequency electron spin resonance study of T4 lysozyme dynamics using the slowly relaxing local structure model. *J Phys Chem B* 108(45):17649–17659.
5. Möbius K, et al. (2005) Combining high-field EPR with site-directed spin labeling reveals unique information on proteins in action. *Magn Reson Chem* 43(Spec no):S4–S19.
6. Kusnetzow AK, Altenbach C, Hubbell WL (2006) Conformational states and dynamics of rhodopsin in micelles and bilayers. *Biochemistry* 45(17):5538–5550.
7. Guo Z, Cascio D, Hideg K, Kálái T, Hubbell WL (2007) Structural determinants of nitroxide motion in spin-labeled proteins: Tertiary contact and solvent-inaccessible sites in helix G of T4 lysozyme. *Protein Sci* 16(6):1069–1086.
8. Guo Z, Cascio D, Hideg K, Hubbell WL (2008) Structural determinants of nitroxide motion in spin-labeled proteins: Solvent-exposed sites in helix B of T4 lysozyme. *Protein Sci* 17(2):228–239.
9. Lietzow MA, Hubbell WL (2004) Motion of spin label side chains in cellular retinol-binding protein: Correlation with structure and nearest-neighbor interactions in an antiparallel beta-sheet. *Biochemistry* 43(11):3137–3151.
10. Fleissner MR, Cascio D, Hubbell WL (2009) Structural origin of weakly ordered nitroxide motion in spin-labeled proteins. *Protein Sci* 18(5):893–908.
11. López CJ, Oga S, Hubbell WL (2012) Mapping molecular flexibility of proteins with site-directed spin labeling: A case study of myoglobin. *Biochemistry* 51(33):6568–6583.
12. Budil DE, Lee S, Saxena S, Freed JH (1996) Nonlinear-least-squares analysis of slow-motion EPR spectra in one and two dimensions using a modified Levenberg–Marquardt algorithm. *J Magn Reson A* 120(2):155–189.
13. Altenbach C, Oh KJ, Trabanino RJ, Hideg K, Hubbell WL (2001) Estimation of inter-residue distances in spin labeled proteins at physiological temperatures: Experimental strategies and practical limitations. *Biochemistry* 40(51):15471–15482.
14. Greenfield NJ (2006) Using circular dichroism collected as a function of temperature to determine the thermodynamics of protein unfolding and binding interactions. *Nat Protoc* 1(6):2527–2535.
15. Columbus L, Hubbell WL (2004) Mapping backbone dynamics in solution with site-directed spin labeling: GCN4-58 bZip free and bound to DNA. *Biochemistry* 43(23): 7273–7287.
16. López CJ, Fleissner MR, Guo Z, Kusnetzow AK, Hubbell WL (2009) Osmolyte perturbation reveals conformational equilibria in spin-labeled proteins. *Protein Sci* 18(8):1637–1652.
17. Bridges MD, Hideg K, Hubbell WL (2010) Resolving Conformational and Rotameric Exchange in Spin-Labeled Proteins Using Saturation Recovery EPR. *Appl Magn Reson* 37(1-4):363.
18. McCoy J, Hubbell WL (2011) High-pressure EPR reveals conformational equilibria and volumetric properties of spin-labeled proteins. *Proc Natl Acad Sci USA* 108(4): 1331–1336.
19. Fleissner MR, et al. (2011) Structure and dynamics of a conformationally constrained nitroxide side chain and applications in EPR spectroscopy. *Proc Natl Acad Sci USA* 108(39):16241–16246.
20. Jeschke G, Polyhach Y (2007) Distance measurements on spin-labelled biomacromolecules by pulsed electron paramagnetic resonance. *Phys Chem Chem Phys* 9(16):1895–1910.
21. Pyka J, Ilnicki J, Altenbach C, Hubbell WL, Froncisz W (2005) Accessibility and dynamics of nitroxide side chains in T4 lysozyme measured by saturation recovery EPR. *Biophys J* 89(3):2059–2068.

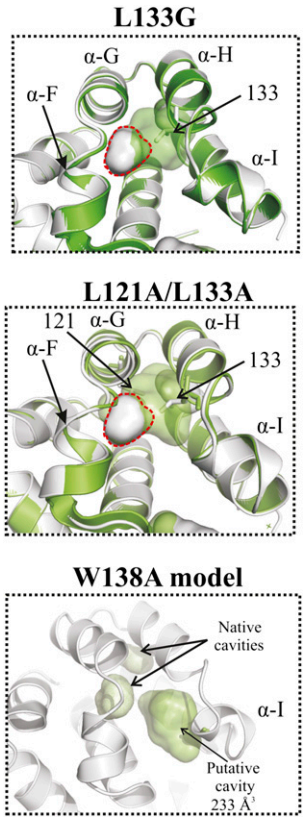

Fig. S1. Overlay of structures of WT (gray ribbon) and mutant (green ribbon) proteins of T4L. X-ray structures of L133G (PDB ID code 226l) and L121A/L133A (PDB ID code 251l) showing the engineered cavity are shown (1, 2). The surfaces of the engineered cavities are shown as green surfaces; the dashed red lines in the top and center panel delineate the boundary of the native cavity I (gray surface). A model of W138A is shown in the bottom panel. The surface of the native cavities I and II are also shown in gray.

1. Xu J, Baase WA, Baldwin E, Matthews B (1998) The response of T4 lysozyme to large-to-small substitutions within the core and its relation with the hydrophobic effect. *Protein Sci* 7:158–177.
2. Baldwin E, Baase WA, Zhang X, Feher V, Matthews BW (1998) Generation of ligand binding sites in T4 lysozyme by deficiency-creating substitutions. *J Mol Biol* 277:467–485.

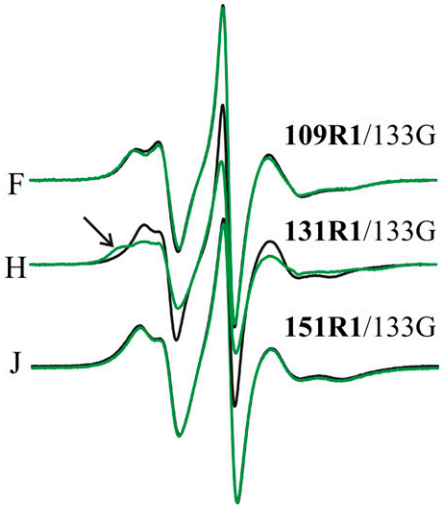

Fig. S2. Effect of L133G mutation in T4L on the spectra of R1. Overlay of the spectra of R1 at the indicated sites for the WT (black traces) and L133G proteins (green traces). The helix in which each site is located is indicated. The arrow identifies a new relatively immobile state of R1.

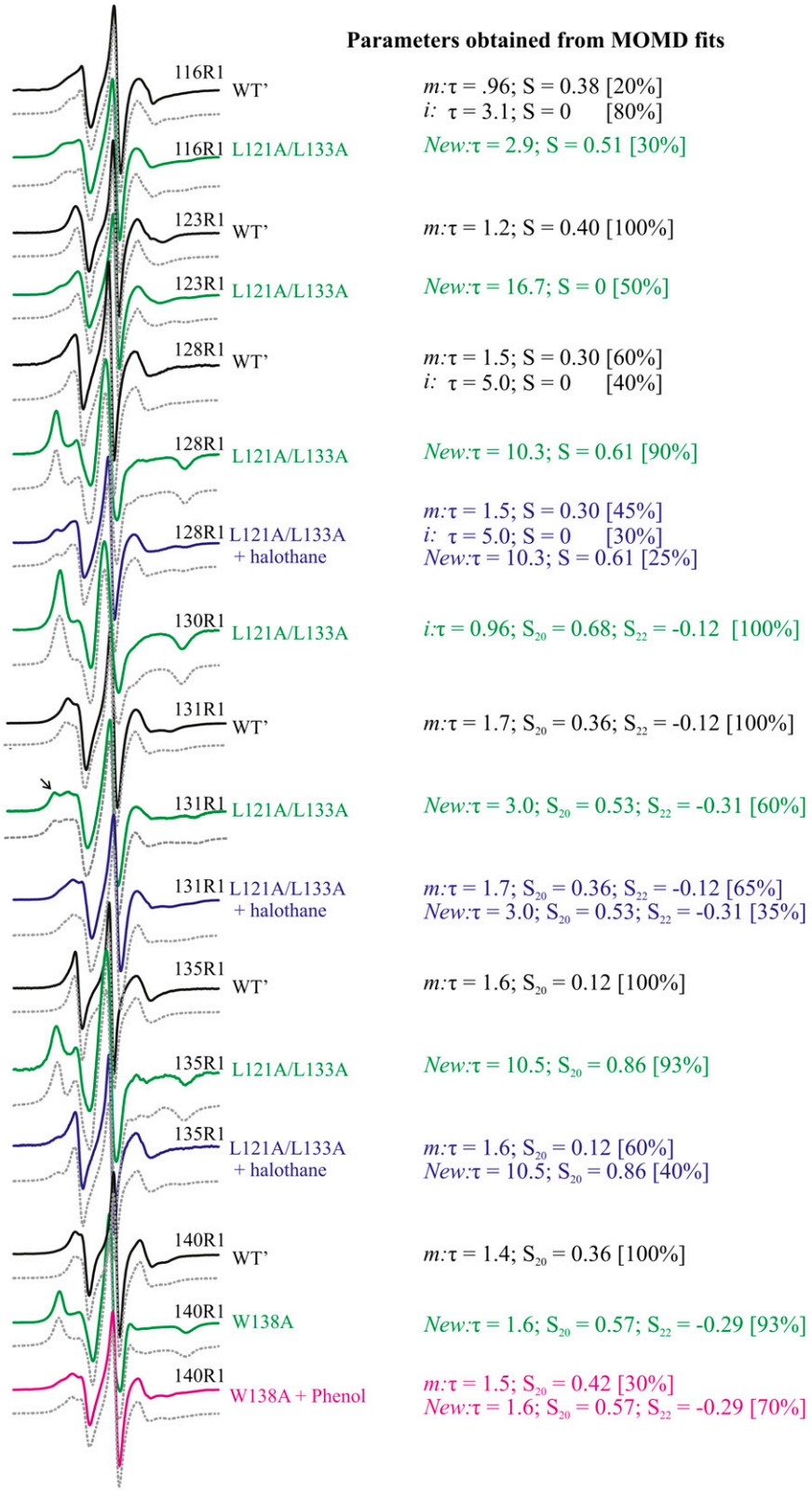

Fig. S3. Simulations of experimental spectra using a one- or two-component MOMD model (*SI Materials and Methods*). The experimental spectra (solid lines) and best fits (gray dashed lines) for the indicated sites are shown along with the effective correlations times (τ), order parameters (S) and populations obtained from the fits; "new" refers to spectral components that are observed only in the presence of the cavity.

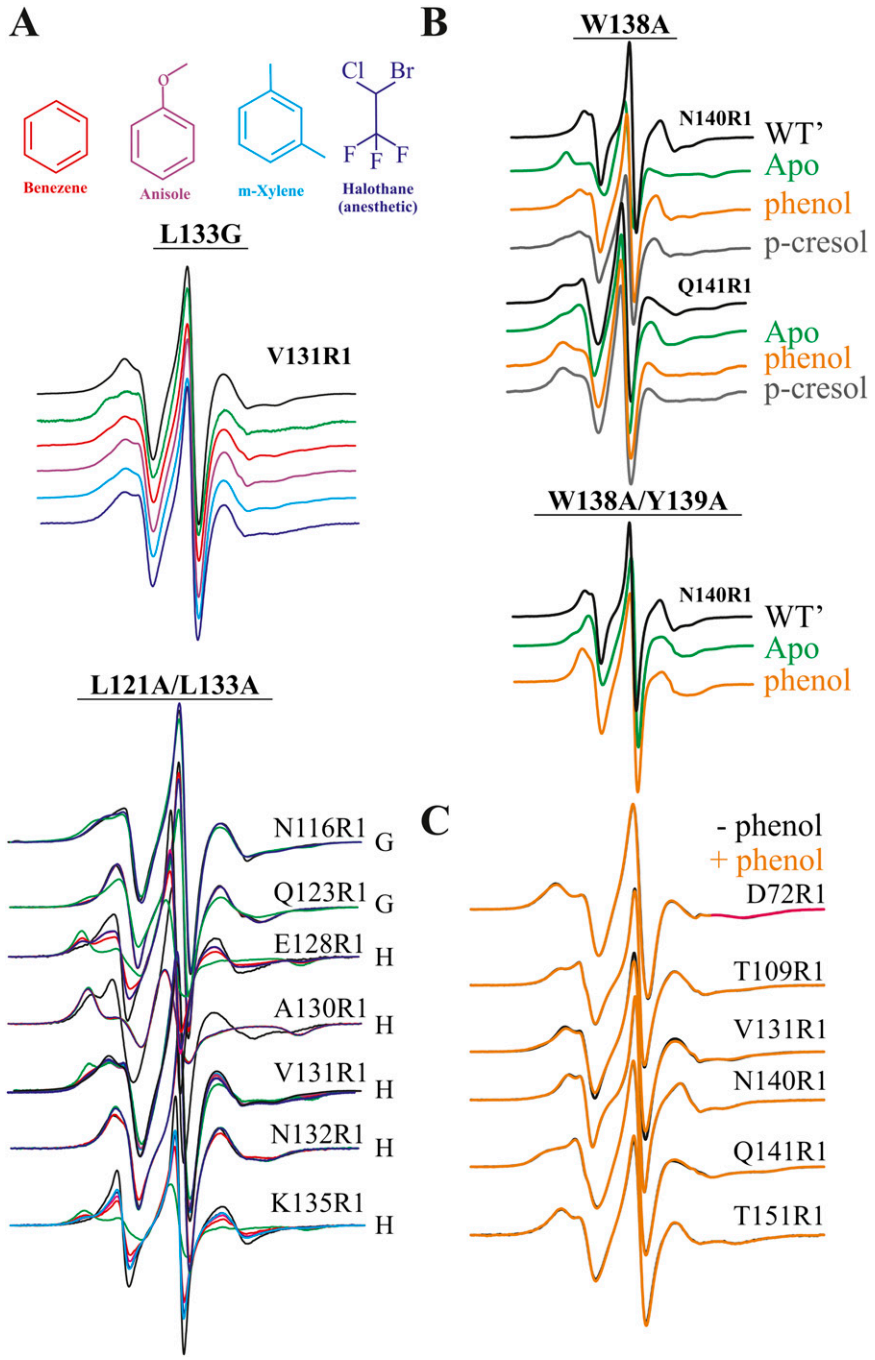

Fig. S4. Effect of ligand binding on the EPR spectra of R1 in T4L cavity mutants. (*A*) Ligand binding to 133G and 121A/133A as detected by R1 at the indicated sites. The EPR spectra for the WT′ proteins (black traces), for the cavity mutants without ligand (green traces) and in the presence of ligand at saturating concentrations (color-coded according to the ligand, *Top*) are shown. For the 121A/133A mutant the helices where the sites are located are indicated. (*B*) Ligand binding to the W138A and W138A/Y139A mutants as detected by R1 at the indicated sites. EPR spectra of the WT′ (black trace), the cavity mutant without ligand (green trace), and in the presence of 50 mM the indicated ligand are provided. (*C*) Effect of 50 mM phenol on the spectra of R1 sites in the WT′ background protein.

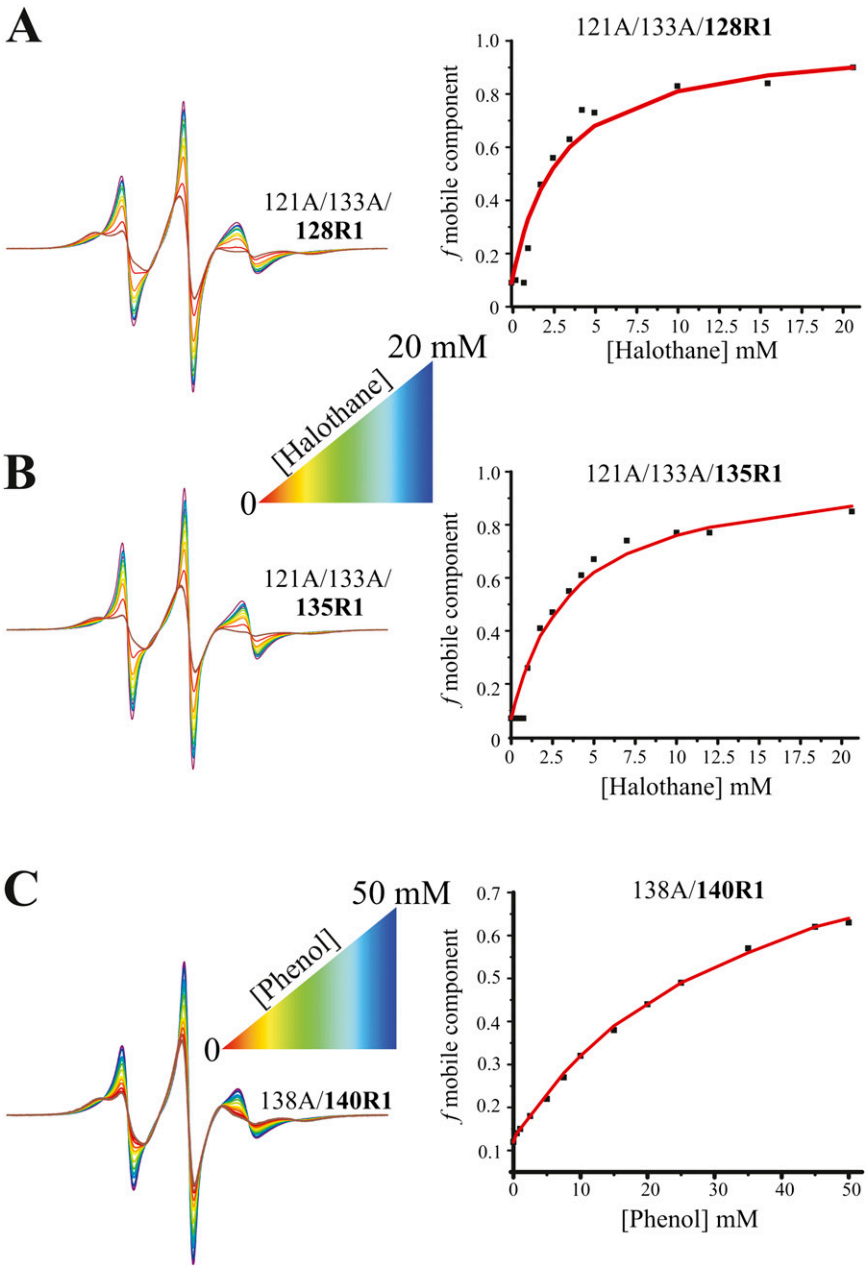

Fig. S5. Ligand titrations of the 121A/133A and 138A cavity mutants detected by R1 sensors. (*A*) EPR spectra of 128R1 in the 121A/133A cavity mutant in buffer (no sucrose) in the presence of increasing concentration of halothane. The spectra are color-coded in a color gradient from red to blue (low to high concentration of ligand). A plot showing the fractional population of the mobile state (*f* mobile) in 128R1/121A//133A as a function of added halothane concentration and a fit of the data to the model in *SI Materials and Methods* with K_1, K_{2d} as parameters is shown in red. *B* and *C* show similar data for 135R1 in the 121A/133A cavity mutant and 140R1 the 138A cavity mutant with phenol as the ligand for the latter. The K_{2d} values obtained from the fits are: 0.26 mM (128R1/L121A//L133A), 0.24 mM (135R1/L121A/L133A), 4.46 mM (phenol; 140R1/W138A), and 4.26 mM (*p*-cresol: 140R1/W138A).

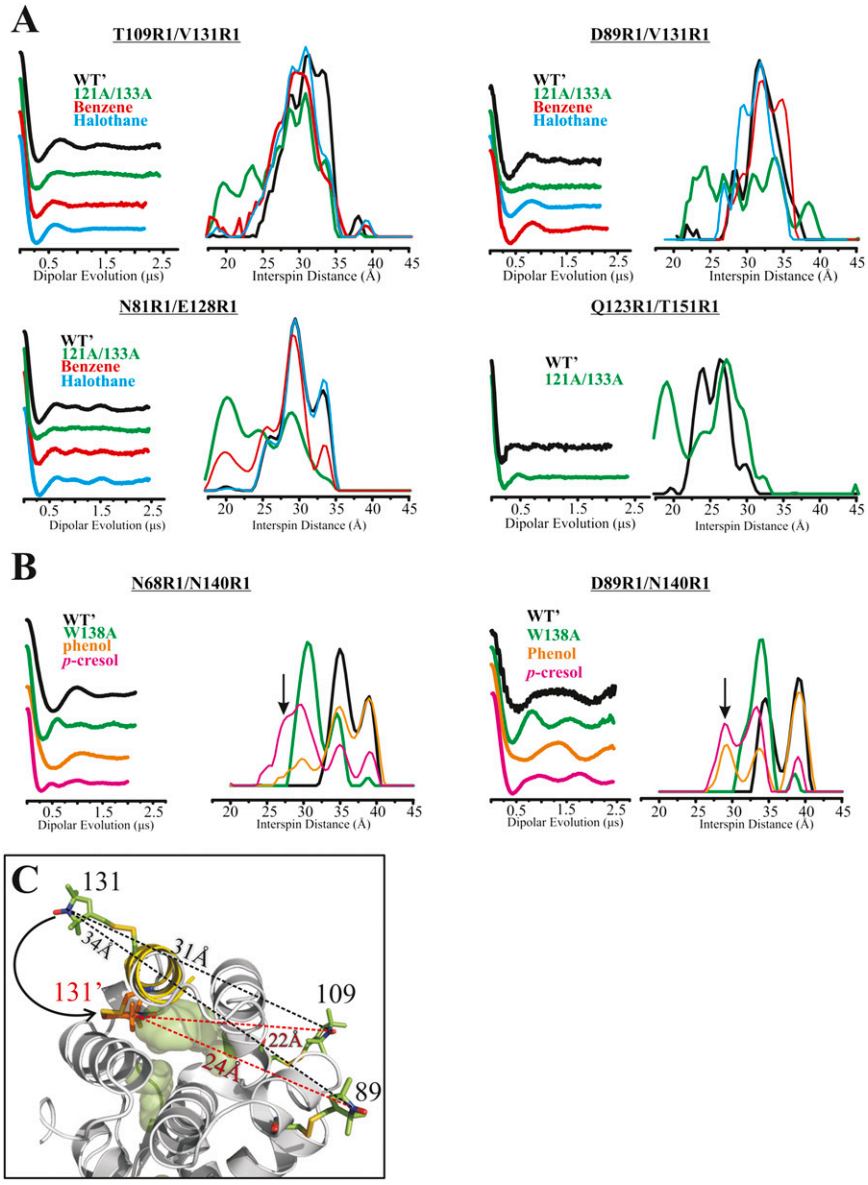

Fig. S6. DEER data on doubly-labeled T4L in the WT′ and cavity mutant background proteins. (*A* and *B*) Background corrected dipolar evolution function (*Left*) and corresponding distance distribution profiles (*Right*) for the indicated doubles in the WT′ and 121A/133A mutant (*A*) and W138A mutant (*B*). The arrows in (*B*) identify new distances populated in the presence of phenol and *p*-cresol. (*C*) A model showing rotation of helix H whereby 131R1 moves to a new position (131′) in the 121A/133A mutant that is compatible with CW data, SR data, and interspin distance measurements. Distances in black are those in WT′ state, while those shown in red indicate distances in the new state.

Table S1. Effect of R1 and halothane binding on the stability of cavity mutants of T4L

Mutant	T_m, °C	ΔT_m, °C, due to labeling	ΔT_m, °C, halothane binding
WT*	54.1	—	—
116C/121A/133A	33.2	—	—
116R1/121A/133A	36.6	3.4	—
116R1/121A/133A + halothane	41.4	—	4.8
123C/121A/133A	34.7	—	—
123R1/121A/133A	37.2	2.5	—
123R1/121A/133A + halothane	40.9	—	3.7
128C/121A/133A	35.3	—	—
128R1/121A/133A	38.1	2.8	—
128R1/121A/133A + halothane	40.7	—	2.6
130C/121A/133A	36.5	—	—
130C/121A/133A + halothane	42.3	—	5.8
130R1/121A/133A	45.0	8.5	—
130R1/121A/133A + halothane	44.9	—	−0.1
130AP/121A/133A	35.3	−1.2	—
130AP/121A/133A + halothane	40.0	—	4.7
131C/121A/133A	38.0	—	—
131R1/121A/133A	40.2	2.2	—
131R1/121A/133A + halothane	42.8	—	2.6
132C/121A/133A	36.8	—	—
132R1/121A/133A	36.1	−0.7	—
132R1/121A/133A + halothane	42.3	—	6.2
135C/121A/133A	38.9	—	—
135R1/121A/133A	41.7	2.8	—
138A/140C	46.7	—	—
138A/140R1	48.5	1.8	—

T4L WT* is pseudo-WT (C54T/C97A). Save for the 116C and 123C mutants, thermal unfolding was >95% reversible. Errors in T_m are ±0.5 °C. AP, acetamidoproxyl.

Table S2. Relevant parameters obtained from SR EPR

Mutant	$T_{1\ fast}$, ns	$T_{1\ slow}$, ns	J_{fast}, MHz/mM	J_{slow}, MHz/mM	Population fast, %	$K_{exchange}$, kHz	1/K, μs
116R1	2,300	n/a	n/a	n/a	n/a	n/a	n/a
116R1/121A/1331	2,100	5,400	0.25	0.001	30*	n/d	n/d
123R1/121A/133A	2,200	4,500	0.20	0.001	58	≤14.3	≥70
128R1/121A/133A	2,300	6,000	0.20	0.006	9	≤14.3	≥70
130R1/121A/133A	n/a	6,610	n/a	<0.001	0	n/a	n/a
130AP/121A/133A	n/a	3,000	n/a	0.074	n/a	n/a	n/a
131R1/121A/133A	1,900	5,500	0.16	0.012	40*	n/d	n/d
135R1/121A/133A	2,000	5,800	0.11	0.002	93*	n/d	n/d
131R1/138A	n/a	3,400	n/a	0.025	n/a	n/a	n/a
140R1/138A	n/a	3,530	n/a	0.100	7*	n/a	n/a

Intrinsic electron spin relaxation time (T_{1e}) values for 128R1, 130R1, 131R1, and 135R1 have been previously reported (1). AP, acetamidoproxyl; n/a, not applicable; n/d, not determined.
*Values shown are from MOMD fits.

1. Pyka J, Ilnicki J, Altenbach C, Hubbell WL, Froncisz W (2005) Accessibility and dynamics of nitroxide side chains in T4 lysozyme measured by saturation recovery EPR. *Biophys J* 89(3): 2059–2068.

Table S3. Interspin distances and distance distributions for doubly labeled T4L in the WT and mutant background proteins

Mutant	R1-R1 distance, Å, from modeling[†]	Experimental R1-R1 distance, Å	Distribution, Å
68R1/130R1	33.0	30.8, 35.0	
81R1/128R1	29.0	29.5	±4.5
81R1/132R1	23.5	24.5	
89R1/131R1*	33.7	31.9	±3.9
109R1/131R1*	31.2	31.4	±4.9
68R1/140R1	35.6	35.0, 39.0	
89R1/140R1	33.5	34.5, 39.0	
109R1/140R1	24.3	24.4	±8.4
140R1/151R1	21.2	21.3	
123R1/151R1	24.6	24.0, 26.3	±5
68R1/130R1/121A/133A	(27.0)	27.3	±3.6
81R1/128R1/121A/133A	(24.4)	20.1, 28.9	
81R1/132R1/121A/133A	(31.1)	19[‡], 31.2[‡]	
89R1/131R1/121A/133A	(24.5)	24.2[‡]	
109R1/131R1/121A/133A	(21.5)	19.5 and 23.5[‡]	
123R1/151R1/121A/133A	n/a	27.2 and 19.0[‡]	
68R1/140R1/W138A	(33.6)	30.5, 34.5	
89R1/140R1/W138A	(33.9)	33.9	±2.6
109R1/140R1/W138A	(29.0)	30.6	±4.2
N140R1/151R1/W138A	(12.6)	12.7 (CW)	

*Distance distributions for these doubles using X-band DEER have been published previously (1) and were repeated for this study at Q-band frequency for comparison.

[†]Distances in parentheses were from modeling of the R1 side chain in the proposed new states shown in Figs. 5 and 8, whereas the rest of the distances represent those modeled in the WT structure. The R1 side chain at sites 81, 130, 131, and 151 was modeled on WT structure using the same dihedral angles observed in the X-ray structures of 81R1, 130R1, 131R1, and 151R1 (2, 3).

[‡]These reported interspin distances are not necessarily the most probable distance in the distribution but rather the new distance observed in the 121A/133A mutant.

1. Fleissner MR, et al. (2009) Site-directed spin labeling of a genetically encoded unnatural amino acid. *Proc Natl Acad Sci USA* 106(51):21637–21642.
2. Fleissner MR, Cascio D, Hubbell WL (2009) Structural origin of weakly ordered nitroxide motion in spin-labeled proteins. *Protein Sci* 18(5):893–908.
3. Fleissner MR (2007) X-ray structures of nitroxide side chains in proteins: A basis for interpreting distance measurements and dynamic studies by electron paramagnetic resonance. PhD dissertation (University of California, Los Angeles).